Environmental Engineering and Management Journal February 2020, Vol. 19, No. 2, 205-217
http://www.eemj.icpm.tuiasi.ro/; http://www.eemj.eu

"Gheorghe Asachi" Technical University of Iasi, Romania

MODELING OF A RECTANGULAR CHANNEL MONOLITH REACTOR FOR SORPTION-ENHANCED WATER-GAS SHIFT

Vlad-Cristian Sandu[1], Ionela-Dorina Dumbrava[1], Ana-Maria Cormos[1], Arpad Imre-Lucaci[1], Calin-Cristian Cormos[1*], Paul Cobden[2], Robert de Boer[3]

[1]*Faculty of Chemistry and Chemical Engineering, Babes-Bolyai University, Arany Janos 11, Cluj-Napoca, RO-400028, Romania*
[2]*Swerim AB, Box 812, SE971 25 Lulea, Sweden*
[3]*TNO Energy Transition, PO Box 15, 1755 ZG, Petten, The Netherlands*

Abstract

As CO_2 concentration levels in the atmosphere are steadily reaching a point of no return, it is paramount that actions are taken towards mitigating emissions by improving the efficiency of existing processes. Sorption-enhanced water-gas shift (SEWGS) combines the water-gas shift reaction with in-situ adsorption of CO_2 on potassium-promoted hydrotalcite (K-HTC). This enables a direct conversion of syngas into separate hot streams of H_2 at feed pressure and CO_2 at regeneration pressure, making the process attractive for pre-combustion carbon capture and storage (CCS) and reduction of greenhouse gas emissions. The current work is evaluating the high-temperature, high-pressure adsorption step of the SEWGS process enhanced by a novel technology which replaces common packed bed reactors with 3D-printed monolithic structures. This approach would enable an overall increase in process productivity. To this extent, innovative dynamic models based on validated competitive adsorption isotherms were developed in this work. COMSOL Multiphysics was used to develop a 1D computational fluid dynamics (CFD) model of adsorption for a fixed bed reactor in order to verify the model accuracy against existing studies. Subsequently, 2D CFD simulations were developed to describe adsorption inside monolith structures, both free and porous regions. The multi-component adsorption isotherm used in the simulations was validated with published breakthrough capacities for CO_2 and H_2O at different pressures. Model predictions are in agreement with expected behavior, as monolith reactors provide a more efficient mass transfer, and will be used to enhance the performance of experimental monolith structures used in SEWGS.

Key words: adsorption isotherm, carbon capture and storage, computational fluid dynamics, sorption-enhanced water-gas shift

Received: January, 2019; Revised final: November, 2019; Accepted: November, 2019; Published in final edited form: February, 2020

1. Introduction

Since the beginning of the Industrial Revolution in eighteenth century Britain, when the increased use of steam power led to thriving metallurgical and chemical industries human activities have continued to negatively impact Earth's climate through the emission of greenhouse gases (GHG). The major anthropogenic GHG is CO_2, which causes the absorption of energy of specific wavelengths that would normally leave the atmosphere to radiate back towards the surface, warming it (Le Treut et al., 2007). Levels of CO_2 emissions in the atmosphere had reached an all-time high in 2010 with a value of almost 400 ppm, accounting for 76% of total anthropogenic GHG emissions. Most CO_2 emissions come from fossil fuel combustion and industrial processes, with electricity and heat production being the leading causes for pollution (IPCC, 2014; Zivkovic et al., 2018). Measures to improve the energy sector and reduce greenhouse gas emissions have been assessed by the Intergovernmental Panel on Climate Change (IPCC). One option for mitigating CO_2 involves a technology known as carbon capture and storage

* Author to whom all correspondence should be addressed: e-mail: cormos@chem.ubbcluj.ro; Phone: +40264 593833

(CCS), which refers to separating CO_2 from industrial point sources and transporting it to storage sites to be deposited. The IPCC outlines three different types of CCS: post-combustion, in which CO_2 is separated from the exhaust of industrial processes, oxyfuel combustion, based on high purity oxygen use, and pre-combustion, a process in which, through water-gas shift, separated carbon dioxide and hydrogen are obtained to be used in combustion or for other purposes (IPCC, 2005).

Hydrogen is valuable due to its role in industrial processes, such as obtaining ammonia and methanol, and shows promise as an efficient, clean source of energy. However, an issue that needs to be addressed is the connection between industrial scale H_2 production and CO_2 emissions (Winter, 2009). A way to achieve both carbon dioxide emissions reduction and hydrogen production is a high potential pre-combustion technology called sorption-enhanced water-gas shift (SEWGS) (Voldsund et al., 2016).

SEWGS is a process that combines the water-gas shift (WGS) reaction (Eq. 1) with in-situ adsorption of CO_2 (Eq. 2) at high-temperatures between 300-500 °C and high-pressure levels between 10-40 bar. Steam adsorption (Eq. 3) is possible based on process conditions (Hufton et al., 1999).

$$CO + H_2O \leftrightarrow CO_2 + H_2 \quad (1)$$
$$CO_2 + \bullet \leftrightarrow CO_2 - \bullet \quad (2)$$
$$H_2O + \bullet \leftrightarrow H_2O - \bullet \quad (3)$$

Conventional WGS technology requires two consecutive reactors to obtain high conversion of CO, followed by pressure swing gas adsorption (PSA) to separate the CO_2 from the pure H_2, whereas with SEWGS, the second reactor and PSA can be combined into a SEWGS unit, leading to less process steps and less equipment needed. Moreover, in the case of a steam methane reformer without carbon capture, the CO_2 is released into the atmosphere, while SEWGS enables high CO_2 capture ratios at a higher energy efficiency and lower cost in comparison with more mature technologies (van Selow et al., 2011).

Considerable efforts were made in testing different sorbents to be used in a SEWGS process, however, most proved to be less desirable for various reasons. Hydrotalcite based adsorbents seem to outclass other types of adsorbents, as they demonstrate high thermal stability, fast sorption kinetics and high CO_2 selectivity (Ebner et al., 2006; Walspurger et al., 2010). The most commonly known hydrotalcite is Mg-Al hydrotalcite (Sikander et al., 2017). The impregnation of the hydrotalcite with alkaline metals, such as K_2CO_3, has been observed to increase the sorbent's capability to adsorb basic species (Lee et al., 2008). The potassium-promoted hydrotalcite (K-HTC) has two roles: acting as catalyst for the WGS reaction and sorbent for reversibly adsorbing CO_2 (Jang et al., 2012; Zheng, et al., 2014). After adsorption, the CO_2 that is released during K-HTC regeneration is sufficiently pure to be stored (Hufton et al., 1999; Lee et al., 2010; Yong et al., 2002).

The SEWGS process (Fig. 1) involves a series of traditional packed bed reactors which run in pressure cycles, enabling the periodic loading and regeneration of the sorbent. Since multiple reactors are being used, the process acts as if continuous and leads to a constant production of separate streams of CO_2 and H_2. In the first cycle step, syngas enters the column in which CO reacts with steam to obtain CO_2 and H_2. CO_2 is taken up by adsorption and a H_2 rich stream is obtained. Once the sorbent is saturated, a medium-pressure steam rinse takes place pushing the syngas into another reactor. After the rinse, a number of pressure equalizations are performed. During this step, the rinse gas in the high-pressure reactor expands and pushes the remaining syngas into a lower pressure reactor. Gas pressure is conserved since the high-pressure reactor that required depressurization will connect to a lower pressure one that needs to be pressurized. In the blowdown step, the pressure in the reactor is rapidly decreased to 1 bar and some CO_2 is released from the sorbent, exiting the reactor with the steam and allowing particle regeneration. By purging the reactor with low-pressure steam, additional CO_2 is released and sorbent regeneration is enhanced. Following pressure equalization with a high-pressure reactor and re-pressurization, the reactor will be ready to undergo the SEWGS process from the beginning. SEWGS is an attractive process for both pre-combustion CCS and GHG emissions reduction since it directly converts syngas into a hot H_2 stream at feed pressure and a separate CO_2 stream at regeneration pressure (Boon et al., 2015). SEWGS appears to be a promising CCS technology, as discussed by Riboldi and Bolland (2017), who highlight the good potential of PSA in pre-combustion applications with hot gas separation processes, especially when considering sorption-enhanced processes.

One bottleneck for traditional fixed bed solutions for sorbent-based CCS technologies is the trade-off between flow-rate through the reactor, pressure drop and kinetics of the adsorption process. A monolith reactor has a honeycomb structure made of thin-walled supports. Many straight parallel channels in micron- and millimeter-scale combine to create the entire structure. These channels can have various shapes, such as square, triangular, circular, hexagonal or others, depending on purpose. In the case of sorption, monolithic structures provide an attractive alternative to regular fixed bed reactors due to the high active surface area of the channels (Govender and Friedrich, 2017). Several fixed bed processes are believed to be able to benefit from the use of monolith configurations, due to pressure drop or mass transfer constraints, as monolithic structures exhibit an outstanding pressure drop to mass transfer ratio (Boger and Sorensen, 2004).

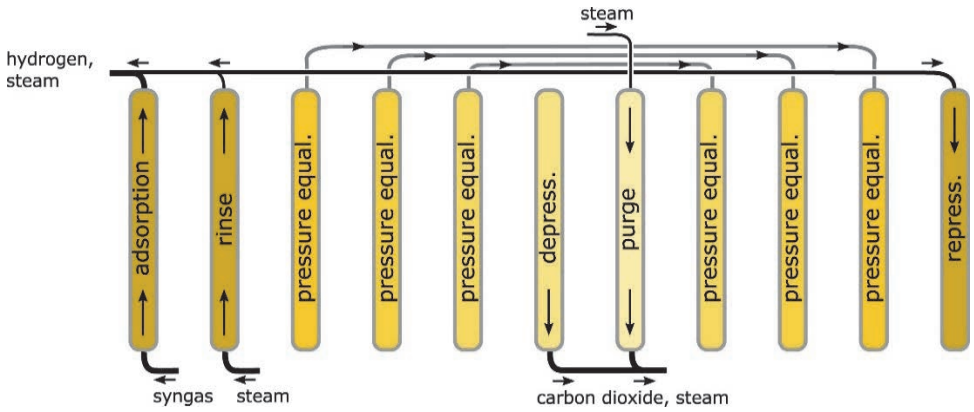

Fig. 1. Eleven step SEWGS cycle with concurrent steam rinse (Boon et al., 2015)

In the last years, the idea of replacing packed bed reactors with monoliths has received more and more attention. The applications that have been proposed include two categories: automobile applications (Dhanushkodi et al., 2008; Sadeghi et al., 2017; Tischer and Deutschmann, 2005) and industrial applications: syngas combustion (Pramanik and Ravikrishna, 2017), benzene alkylation (Dai et al., 2013), PSA (Pahinkar and Garimella, 2018), catalytic oxidation of volatile organic compounds (Rodríguez et al., 2016), Natural Gas Reforming (Heidebrecht et al., 2011), etc. The majority of modeling and simulation research has been focused on gas phase in the monolith, with a small number of papers published on multi-phase monolith reactors (Bertrand et al., 2012; Durán Martínez et al., 2016; Lei et al., 2016).

Depending on the objectives, applications and numerical computational limitations, these models can be classified as 1D, 2D or 3D models (Chen et al., 2008). Based on the monolith structure, there are different modeling scales: single channel (majority of the developed models), multi-channel (Dai et al., 2013; Lupše et al., 2016) or an entire reactor (Bauer et al., 2005).

In order to compare various modeling approaches, the effect of channel geometry (i.e. circle, hexagon, square, rectangle, and regular triangle) on the reactor performance was investigated (Dai et al., 2013, Sadeghi et al., 2017). For monolith catalysts, a regular triangular or rectangular channel shape is favorable when considering pressure drop and process selectivity/conversion. Furthermore, the effect of the most important operating parameters, such as temperature, porosity and wall/wash-coat thickness, inlet velocities, residence time on the conversion in the reactor were investigated by Lupše et al. (2016), Pramanik and Ravikrishna (2017) and Sadeghi et al. (2017).

This paper studies the adsorption step of SEWGS, in which the traditional fixed bed configuration is replaced with monolith structures made of K-HTC adsorbent material. To date, there are few articles published regarding SEWGS modeling and even less on monolith computational fluid dynamics (CFD) simulations for hydrogen production. Reijers et al. (2009a, 2009b) developed a 1D model to study a sorption-enhanced reaction process for CO_2 capture with steam methane reforming (SMR) and WGS reactions taking place in the packed bed reactor, then validated the model based on experimental data. A SEWGS model on packed bed reactors was developed for IGCC by Wright et al. (2011) to investigate the effects of using different feedstocks and discovered that steam amount needed to operate SEWGS units was similar when using syngas from either natural gas or coal. Boon et al. (2014) developed a SEWGS reactor model which uses the linear driving force (LDF) approximation and double component isotherm to accurately predict breakthrough performance and highlight competitive adsorption between CO_2 and H_2O in SEWGS. Irani et al. (2011) developed a CFD model of SMR and WGS in monolith reactors for hydrogen production, but their model was steady state with the purpose of investigating efficiency of surface or volume-based reaction models in terms of better predictions.

In this work, CFD models were developed in COMSOL Multiphysics to simulate adsorption of CO_2 and H_2O, the first step of SEWGS, in space-time. For validation purposes, a 1D model of a fixed bed reactor was developed to enable comparison to existing published data. Subsequently, a 2D model considering mass, heat and momentum transfer was built to simulate adsorption inside a single channel of a monolith reactor. As no experimental data was available on such configurations, pre-validation was done through analytical methods. The key target was using CFD for assessment of adsorption kinetics in structured bed configurations for SEWGS.

2. Model development

2.1. Breakthrough measurements

Boon et al. (2014) performed breakthrough experiments in a multi-column SEWGS test rig, which was accurately described by van Selow et al. (2009). H_2O breakthrough capacity was measured at three total pressure levels: 8, 17.5 and 27 bar(a). At each of the pressure levels, breakthrough measurements were carried out with 11, 43 and 78 volume percentage of steam in argon-nitrogen gas mixture. Subsequently,

CO_2 breakthrough experiments were performed at 7, 12, 17, 22 and 27 bar(a) total pressure. The volume percentages of CO_2 in argon-nitrogen mixture were 3, 33 and 71 for every pressure setting. The CO_2-H_2O mixture breakthrough experiments were aimed at measuring excess adsorption of CO_2 and H_2O at 400 °C and 27 bar(a). In total, 32 conditions were tested with CO_2 partial pressures ranging between 0.5-24 bar and H_2O partial pressures ranging between 4-24 bar.

2.2. Adsorption isotherm

Boon et al. (2014) managed to fit a multi-component adsorption isotherm to the SEWGS system. A model based on two double isotherms was derived to take into account surface contributions and nanopores contributions for CO_2 and H_2O adsorption at high pressures. The regressed parameters are shown in Table 1. Although the surface sites are specific, either adsorbing CO_2 or H_2O, competitive adsorption in nanopores is likely to take place. The surface adsorption of CO_2 was described by a Langmuir isotherm (first term on right side in Eq. 4), in agreement with most other studies found in literature. For the surface contribution of H_2O, a Freundlich isotherm was used (first term on right side in Eq. 5), as to reflect the heterogenous character of the sites for H_2O. Nanopore contribution of both CO_2 and H_2O was described through a Dubinin-Astakhov equation (second term on right side in Eqs. (4-5)) based on volume filling theory, where the assumption of no lateral interactions between adsorbed species enabled the amount of gas adsorbed to be determined by the limiting nanopore volume V_0, pore-size distribution parameter m and the nanopore-sorbate interaction energy E (Do, 1998; Coenen et al., 2017). As such, in the case of CO_2 (Eq. 4):

$$q^*_{CO_2} = \frac{q^s_{CO_2} K_{CO_2} p_{CO_2}}{1+K_{CO_2} p_{CO_2}} + \frac{A_{CO_2}(V_0 - V_0 A_{H_2O})}{v_{m,CO_2}(1-A_{CO_2} A_{H_2O})} \quad (4)$$

$$q^*_{H_2O} = K_{H_2O} p^{1/n}_{H_2O} + \frac{A_{H_2O}(V_0 - V_0 A_{CO_2})}{v_{m,H_2O}(1-A_{CO_2} A_{H_2O})} \quad (5)$$

where:

$$A_i = exp\left(-\left[\left(\frac{RT}{E_i}\right) ln\left(\frac{p_{0,i}}{p_i}\right)\right]^{m_i}\right) \quad (6)$$

$$p_{0,i} = p_{c,i}\left(\frac{T}{T_{c,i}}\right)^2 \quad (7)$$

$$v_{m,i} = \frac{RT_{c,i}}{8p_{c,i}}\left(\frac{T}{Tc,i}\right)^{0.6} \quad (8)$$

The values presented in Table 1 were in agreement with values published by other groups. For CO_2 adsorption on K-HTC, Lee et al. (2007) reported similar a monolayer capacity $q^s_{CO_2}$ between 0.25-0.45 mol kg^{-1}, but much higher gas-solid interaction parameter K_{CO_2} at 400 °C in the range of 167 - 369 MPa^{-1}. However, in a study by van Selow et al. (2013), the value reported was 44.5 MPa^{-1}. For H_2O adsorption, the Freundlich exponent n, quantifying the nonlinearity of the isotherm, has been reported to be within the range of 1.7-5.1 on various clays (Hatch, Wiese, Crane, Harris, Kloss, & Baltrusaitis, 2012). Maroño et al. (2013, 2014) found nanopore volumes in the range of 50-60 cm^3 kg^{-1}. The parameter m, which characterizes nanopore heterogeneity, has been found to usually vary between 1-6 (Do, 1998). The characteristic energy E values for CO_2 and H_2O are regular values for nanopore-sorbate energies using the Dubinin-Astakhov model (Do, 1998).

Table 1. Regressed multi-component isotherm parameters used in Eqs. (4-8) (Boon et al., 2014)

Parameter	***Estimate***
$q^s_{CO_2}$ [mol kg^{-1}]	0.45 ± 0.13
K_{CO_2} [MPa^{-1}]	28 ± 26
E_{CO_2} [kJ mol^{-1}]	23 ± 1
m_{CO_2} [-]	5.2 ± 1.5
K_{H_2O} [mol kg^{-1} MPa$^{-1/n}$]	0.37 ± 0.07
n [-]	1.9 ± 0.5
E_{H_2O} [kJ mol^{-1}]	12 ± 1
m_{H_2O} [-]	3.6 ± 0.8
V_0 [cm^3 kg^{-1}]	74 ± 17

2.3. Reactor models

2.3.1. Fixed bed reactor model

To investigate the kinetics of adsorption, Boon et al. (2014) developed a reactor model based on a previous reactor model for low-pressure sorption-enhanced reforming published by Reijers et al. (2009). With the purpose of validation, a 1D model simulating adsorption in a fixed bed reactor with sorbent pellets was carried out in the current work. The model was built with COMSOL Multiphysics, using the Chemical Reactions and Engineering Module, which enabled simulation of transport in porous media. Discretization of the porous domain was done using a custom made extremely fine mesh, calibrated for fluid dynamics. Since the model was one dimensional, only the x-coordinate was taken into account. The transport equation in the bulk (Eq. 9) accounted for the combined effects of convection and diffusion:

$$\frac{\partial c_i}{\partial t} + \nabla \cdot (-D_i \nabla c_i) + u \cdot \nabla c_i = R_i \quad (9)$$

where, the first term described the rate of change in concentration with respect to time, the second was the diffusive term and the third the convective term. The reaction rate term R_i was 0.

The transport equations in the porous domain (10) accounted for effective diffusion and convection: where the first and second terms describe the rate of change in concentration and bed porosity, respectively, with respect to time, the third term was the effective diffusivity and the fourth was the convective term. Again, the value for the reaction rate

term R_i was 0. Eqs. (11-14) used for the intraparticle model are based on the common LDF assumption for porous spherical particles (Table 2) (Reijers et al., 2009a). Eq. 11 shows the rate of change in loading amount with respect to time, proportional with the mass transfer coefficient k_{LDF} (Eq. 12), with two components accounting for pore diffusion (Eq. 13) and surface diffusion (Eq. 14). Model dimensions and process conditions are presented in Table 3.

2.3.2. Structured bed reactor model

A graphical representation of the monolith structure with square channels considered in this work is presented in Fig. 2a and a single channel is shown in Fig. 2b. The monolith reactor's axial section was considered circular. The number of possible channels was based on the channel dimensions and reactor surface. By assuming that the flow was evenly distributed within the monolith structure and that each channel was identical, it was possible to characterize the entire monolith by studying just one channel (Chen et al., 2008; Sharma and Birgersson, 2016). The channel's axial section was considered square. The transition from 3D to 2D was decided based on having less model complexity, which translates into less computation time and hardware requirements needed to run the simulations. Model dimensions are shown in Table 4.

The wall thickness corresponding to each channel was obtained by assuming that the entire surface of adsorbent is equally active, including near the edges of the reactor where diffusion effects might be weaker, thus dividing the surface available of adsorbent by the number of channels.

The high length-width ratio between the reactor length of 1 m and channel width of 1 mm led to a complicated meshing process. However, the mesh was finely discretized with special focus on the transition zone between the inlet section with slip wall condition and free channel, the boundaries between free channel and the porous domain itself. Error tolerances were also tightened accordingly to obtain accurate predictions. Relative error values were below 10^{-4} for all solved variables.

The following assumptions were considered for the 2D monolith reactor simulation:

1. Uniform distribution of sorbent activity;
2. Dynamic mixture, thermodynamic and transport properties;
3. Convection and diffusion in the bulk and porous media (Fick's Law);
4. Compressible laminar fluid flow;
5. Heat transfer in the fluid and porous media;
6. WGS was not considered;
7. Adsorption of CO_2 and H_2O were taken into account (surface and nanopore contributions);
8. Porous mass transfer resistance calculated with LDF approximation.

The equations used in the mathematical model are presented in Table 5. The fluid was considered as being compressible with a time dependent density, which led to the continuity equation (Eq. 15).

$$\left(\boldsymbol{\varepsilon_b} + \boldsymbol{\rho_b k_{p,i}}\right)\frac{\partial \boldsymbol{c_i}}{\partial \boldsymbol{t}} + \left(\boldsymbol{c_i} - \frac{\boldsymbol{\rho}}{\boldsymbol{(1-\varepsilon_b)}}\boldsymbol{c_{p,i}}\right)\frac{\partial \boldsymbol{\varepsilon_b}}{\partial \boldsymbol{t}} + \boldsymbol{\nabla}\cdot\left(-\boldsymbol{D_{e,i}}\boldsymbol{\nabla c_i}\right) + \boldsymbol{u}\cdot\boldsymbol{\nabla c_i} = \boldsymbol{R_i} \quad (10)$$

Table 2. Intraparticle equations (Eqs. 11-14)

Species i adsorption reaction rate	$\frac{\partial q_i}{\partial t} = k_{LDF}\cdot(q_i^* - q_i)$	(11)
LDF mass transfer coefficient	$k_{LDF} = k_{LDF}^{pore} + k_{LDF}^{surf}$	(12)
k_{LDF} for pore diffusion	$k_{LDF}^{pore} = \frac{15D_s}{(d_p/2)^2}\frac{\varepsilon_p}{\varepsilon_p + (1-\varepsilon_p)\rho_p RT(\partial q_i^*/\partial p_i)}$	(13)
k_{LDF} for surface diffusion	$k_{LDF}^{surf} = \frac{15D_s}{(d_p/2)^2}\frac{\rho_p RT(\partial q_i^*/\partial p_i)}{\varepsilon_p + (1-\varepsilon_p)\rho_p RT(\partial q_i^*/\partial p_i)}$	(14)

Table 3. Fixed bed model dimensions and process conditions (Reijers et al., 2009a)

Parameter	***Value***	***Parameter***	***Value***
L [m]	0.2	d_p [m]	3.15e-4
h [m]	0.02	ε_b [-]	0.4
d [m]	0.016	ε_p [-]	0.07
u_f [m s^{-1}]	0.0056	ρ_b [kg m^{-3}]	553
p_f[Pa]	101325	ρ_p [kg m^{-3}]	922
T_f [K]	673.15	y_{CO_2} [-]	0.05
D_m [m^2 s^1]	7.4e-5	y_{H_2O} [-]	0.29
D_p [m^2 s^{-1}]	1.2e-6	y_{N_2} [-]	0.66
D_s^0 [m^2 s^{-1}]	1.5e-10	k_{LDF} [-]	0.1

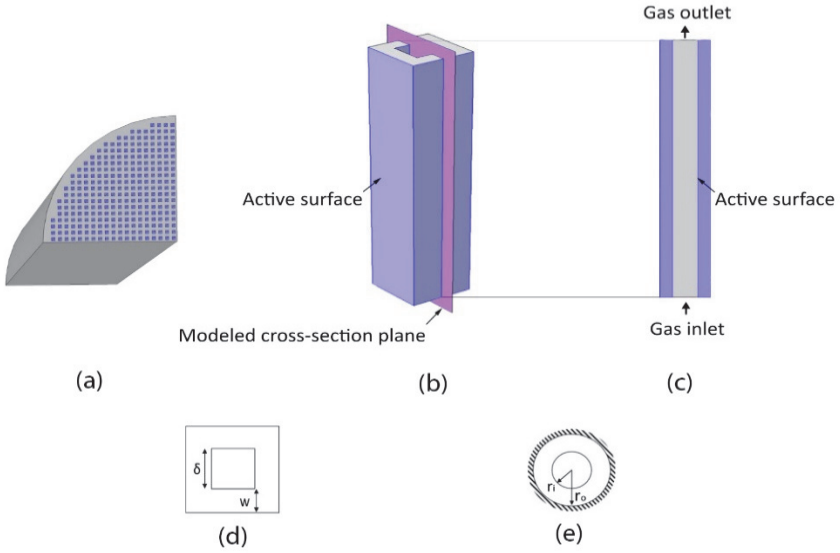

Fig. 2. 3D schematic representation of a monolith reactor with straight square channels (a), 3D representation of a single channel (b), 2D geometry used in models (c), channel axial section (d), hollow cylinder with insulated external surface (e) (Patton et al., 2004)

Table 4. Structured bed model dimensions and process parameters

Parameter	***Value***	***Parameter***	***Value***
L [m]	1	ε [-]	0.57
d_R [m]	0.038	ρ_m [kg m^{-3}]	1848
d [m]	0.001	$\Delta H_{co_2}^{ads}$ [J mol^{-1}]	-65000
wt [m]	0.000573	$\Delta H_{H_2O}^{ads}$ [J mol^{-1}]	-50000
nc [-]	457	C_p [J kg^{-1} K^{-1}]	1048
L_{inlet} [m]	0.25	K [m^2]	1e-12
Q_V [SL/min]	20	y_{CO} [-]	0.03
u_f [m s^{-1}]	0.029	y_{H_2} [-]	0.6
p_f[Pa]	25e5	y_{CO_2} [-]	0.13
T_f [K]	673.15	y_{H_2O} [-]	0.21
D_m [m^2 s^1]	3.85e-6	y_{N_2} [-]	0.03

The vector fields were considered only for directions x and y. Mass transport in the bulk was solved by using a convection-diffusion equation (Eq. 16), while mass transport inside the porous domain was modeled with a porous media transport equation (Eq. 17). Adsorption of CO_2 and H_2O took into account the double-component isotherm (Eqs. (4-5)) and was solved by Eq. 18, using a dynamic k_{LDF}, considered a sink in the mass transport equation inside the porous media (Eq. 17).

Fluid flow was modeled with the Navier-Stokes equations for laminar flow in the bulk (Eq. 19), which accounted for fluid velocity, fluid pressure, fluid density and fluid dynamic viscosity. The term on the left-hand side corresponded to momentum transferred by convection in free flow, while the term on the right-hand side corresponded to pressure and viscous forces. The Forchheimer corrected Brinkman equations (Eq. 20) were used for flow inside the porous domain, which also accounted for the permeability of the porous medium, the porosity and a friction coefficient C_f (Eq. 21). The term on the left-hand side represented a contribution associated with the drag force experienced by the fluid flowing through a porous medium. Additionally, the last term on the right-hand side presented the Forchheimer correction (Eq. 22) to account for turbulent drag contributions to the resistance to flow in the porous domain. Boundary conditions are a flat inlet velocity at the channel entrance based on the channel area and desired flow rate, no slip condition at the walls and a pressure condition with suppressed backflow at the channel exit. In order to avoid inconsistent boundary conditions, an inlet section with assumed symmetry prescribing no penetration and vanishing shear stresses was added to the geometry.

Heat transfer in the fluid was modeled by Eq. 23, while heat transfer in the porous domain was calculated with Eq. 24. Due to fluid motion, convective and conductive contributions were included in the heat transfer equations (Eqs. (23-24)). The conductive heat flux, describing gas-solid heat transfer, was proportional to the temperature gradient (Eq. 25). Heat transfer in porous media had an additional term for adsorption related heat source Q (Eq. 24). The SEWGS process took place after a SMR reactor, followed by a pre-shift process, which can be noticed in the inflow gas composition (Table 4). Based

on the compositions, the WGS reaction was considered negligible. The main focus of the simulation was investigating the adsorption process and without the WGS reaction, the calculation of a stoichiometric breakthrough time to verify adsorption was possible.

Another key difference separating the monolith structure from the fixed bed reactor was the LDF mass transfer coefficient. A different expression (Eq. 26) was used to calculate the mass transfer coefficient k as a function the monolith wall thickness w and channel width δ. Since the shape of the monolith channels in this work was considered square (Fig. 2d), it was possible to transform the geometry into an equivalent cylinder, such as a hollow cylinder with insulated external surface (Fig. 2e), the surface representing halfway inside the monolith wall where internal loading was zero. The transformation allowed the use of the LDF approximation for cylinders (Eq. 31) (Patton et al., 2004).

3. Results and discussions

3.1. Breakthrough capacities for CO_2 and H_2O

The adsorption capacities for CO_2 and H_2O have been derived from the breakthrough experiments. The data points in Fig. 3 show CO_2-H_2O mixture breakthrough capacities. The lines are drawn based on the isotherm developed from the full dataset, described earlier in detail in the paper, while the diamonds mark experimental data.

Pure CO_2 capacities can be explained by a two-step adsorption mechanism. Adsorption of up to 0.4 mol kg-1 is attributed to surface sites, while the rest at pressures above 3 bar is due to nanopores.

Table 5. Structured bed model equations

Continuity	$\frac{\partial \rho}{\partial t} \nabla \cdot (\rho u) = 0$	(15)
Mass transfer in bulk	$\frac{\partial c_i}{\partial t} + \nabla \cdot (-D_i \nabla c_i) + u \cdot \nabla c_i = 0$	(16)
Mass transfer in solid	$(\varepsilon + \rho_m k_{p,i}) \cdot \frac{\partial c_i}{\partial t} + \left(c_i - \frac{\rho}{(1-\varepsilon)} \cdot c_{p,i}\right) \frac{\partial \varepsilon}{\partial t} + \nabla \cdot (-D_{e,i} \nabla c_i) + + u \cdot \nabla c_i = R_{ADS,i}$	(17)
Adsorption rate	$R_{ADS,i} = \frac{dq_i}{dt} = k_{LDF} \cdot (q_i^* - q_i)$	(18)
Momentum in bulk	$\rho \frac{\partial u}{\partial t} + \rho(u \cdot \nabla)u = \nabla \cdot \left[-pI + \mu\left(\nabla u + (\nabla u)^T - \frac{2}{3}\mu(\nabla \cdot u)\right) I\right]$	(19)
Momentum in solid	$\frac{1}{\varepsilon}\rho \frac{\partial u}{\partial t} + \frac{1}{\varepsilon}\rho(u \cdot \nabla)u \frac{1}{\varepsilon} = \nabla \cdot [-pI + \mu \frac{1}{3}(\nabla u + (\nabla u)^T - - \frac{2}{3}\mu \frac{1}{\varepsilon}(\nabla \cdot u) I] - \left(\mu K^{-1} + \beta_F \lvert u \rvert + \frac{\nabla \cdot (\rho u)}{\varepsilon^2}\right) u$	(20)
Friction coefficient	$C_F = \frac{1.75}{\sqrt{150\varepsilon^3}}$	(21)
Forchheimer coefficient	$\beta_F = \frac{\rho \varepsilon C_f}{\sqrt{K}}$	(22)
Heat transfer in fluids	$d_z \rho C_p \frac{\partial T}{\partial t} + d_z \rho C_p u \cdot \nabla T + \nabla \cdot q = q_0$	(23)
Heat transfer in solids	$d_z (\rho_m C_{p,m})_{eff} \frac{\partial T}{\partial t} + d_z \rho_m C_{p,m} u \cdot \nabla T + \nabla \cdot q = d_z Q + q_0$	(24)
Conductive heat flux	$q = -d_z k \nabla T$	(25)

$$k = \frac{4}{k_1 - k_2} \tag{26}$$

where:

$$k_1 = \left(\frac{r_o}{r_i} - 1\right) \cdot (r_o^2 - r_i^2) \tag{27}$$

$$k_2 = \left(\frac{1}{r_i \cdot (r_o - r_i)}\right) \cdot \frac{1}{2}(r_o^4 - r_i^4) - \left(\frac{4}{3} r_o\right) \cdot (r_o^3 - r_i^3) + r_o^2 \cdot (r_o^2 - r_i^2) \tag{28}$$

$$r_i = \frac{2\delta}{\pi} \tag{29}$$

$$r_o = \sqrt{\frac{4w}{\pi}(w + \delta) + r_i^2} \tag{30}$$

$$k_{LDF} = k \cdot D_s \cdot \frac{\varepsilon_p}{\varepsilon_p + (1 - \varepsilon_p)\rho_p RT(\partial q_i^* / \partial p_i)} \tag{31}$$

A similar behavior is seen for pure H_2O capacities. At pressures below 12 bar, experimental data shows the surface contribution around 0.3 mol kg^{-1}. The one point around 20 bar can be attributed to nanopore contribution. Overall, considering the full partial pressure range, the trend in steam adsorption matches the trend observed by Hatch et al. (2012) and supports the idea of a binary adsorption mechanism.**Error! Reference source not found.** demonstrates the importance of the sorbent's nanostructure, especially at higher partial pressures. An indicator towards this is how the impact of CO_2 on the capacity of H_2O is much stronger than the reverse. The larger molar volume of CO_2 in comparison to that of H_2O ensures that the available nanopore volume is more strongly taken up by CO_2 than by H_2O.

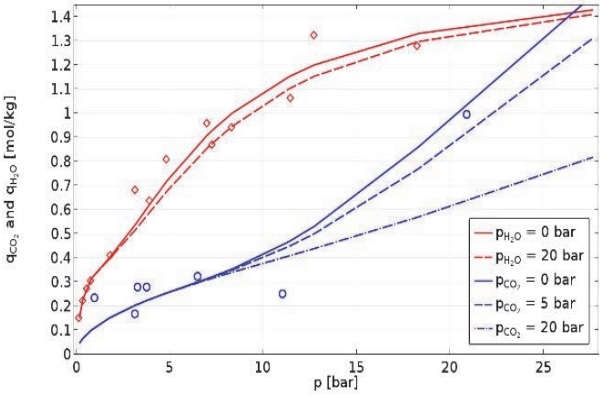

Fig. 3. CO_2-H_2O breakthrough capacities for CO_2 (red diamonds) and H_2O (blue circles) versus partial pressure, predicted pure component capacities (line) and mixture capacities (dashed lines). The experimental dataset obtained by Boon et al. (2014) was used to plot the breakthrough capacities in COMSOL Multiphysics

3.2. Fixed bed reactor model describing CO_2 adsorption

The 1D fixed bed model simulated the adsorption of CO_2 during SEWGS with process conditions shown in Table 3. Fig. 4 presents the comparison between the breakthrough curve published by Reijers et al. (2009a) and the CFD model predicted breakthrough. The CFD model predictions were in accordance with expected behavior, as when compared to the published data, the breakthrough times are within close range, of around 500 s, and the breakthrough curves show nearly identical profiles. The fixed bed model is considered successfully validated.

3.3. Structured bed reactor model describing CO_2 and H_2O adsorption in a single channel

The geometry of the channel used in the 2D model, which had a square cross section and a rectangular longitudinal section, can be seen in Fig. 2c with the addition of an inlet section in order to avoid inconsistent boundary conditions. The dimensions and process conditions can be found in Table 4. The breakthrough curve obtained by the model is presented in Fig. 5a and a summary of results in Table 6.

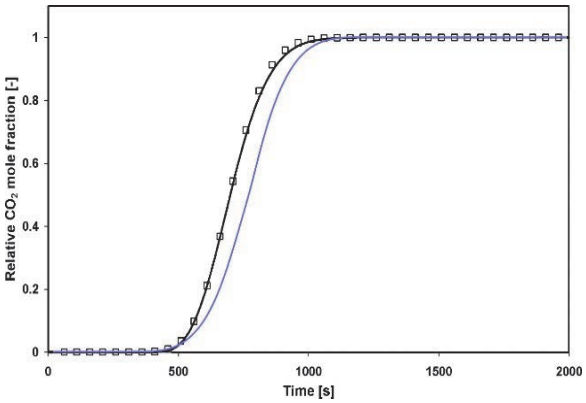

Fig. 4. CO_2 mole fraction at the reactor outlet relative to CO_2 mole fraction of the feed gas. Black – published by Reijers et al. (2009a), line - MATLAB model, symbols - analytical solution; Blue – calculated by the CFD model for a constant k_{LDF} = 0.1 s^{-1}

The total simulated breakthrough time taken at a relative CO_2 mole fraction of 0.95 (Fig. 5a) was 150 s, but the simulation included flow through the inlet section where no adsorption took place. Accounting for the time needed to travel the 250 mm slip wall conditioned inlet section of 8.62 s, the actual CFD model predicted breakthrough time was 141.38. Since the only sink or source of CO_2 was the adsorption process, it was possible to verify accuracy of the predicted loading amount by calculating the stoichiometric breakthrough time:

$$t^* = \frac{q_{CO_2} \cdot m_{ads}}{Q_M} \tag{32}$$

where, q_{CO_2} was the loading amount at breakthrough for $C_{out}/C_{in} = 0.95$ predicted by the CFD simulation (Wood, 2002).

Based on the values of the predicted breakthrough time and analytically calculated stoichiometric breakthrough time (Table 6), the predicted loading amount of CO_2 and accuracy of the model were verified successfully.

The laminar profile of CO_2 flow in the free flow region and the diffusion dominating porous media flow can be seen in Fig. 5b. While convective flow is present in the porous media, its contribution with values of 10^{-6} m/s was negligible. As a result, diffusion dominated porous media flow.

The CFD model predicted a relative CO_2 mole fraction at breakthrough of 0.95 instead of an expected value of 1. This can be explained by the effects related to heat transfer. While breakthrough was achieved, the adsorption process was not entirely completed. As the CFD model simulated the adsorption process over a longer time period (Fig. 6), the relative CO_2 mole fraction reached a value of 1, at which point the adsorbent was completely saturated.

The interdependency of all simulated phenomena is highlighted in Fig. 7 where surface graphs for temperature T K, CO_2 loading amount qCO_2 mol kg^{-1} and H_2O loading amount qH_2O mol kg^{-1} are represented at different time values. The strong impact of heat transfer over the adsorption process can also be observed. As the fluid traveled the channel and diffused into the porous material, the adsorption of CO_2 led to a rise in temperature since the adsorption process was exothermic. At some point, as adsorption took place further into the reactor channel, the continuous inflow of fluid at initial temperature influenced the system closer to the inlet by cooling it. The lower temperature of the adsorbent material increased the adsorption capacity and triggered additional adsorption of CO_2 and desorption of H_2O, highlighting the competitive nature of adsorption in this process.

These effects are in agreement with predictions by the adsorption isotherms (Fig. 3). An isothermal model was developed to verify the predictions of the CFD model regarding heat transfer effects. The breakthrough curve is presented in Fig. 8. The relative CO_2 mole fraction reached a value of 1 during the initial breakthrough because, without heat transfer, no additional adsorption is triggered.

Breakthrough occurred at around 200 s, much later when compared to the non-isothermal model. Without the temperature increase due to exothermic effects, the adsorption capacity was at its highest capacity during the entire process, meaning more CO_2 to be adsorbed and a longer time until breakthrough. Mass transfer efficiency can be investigated by studying the mass transfer zone (MTZ) behavior and length. MTZ graphs at different simulation times are seen in Fig. 9.

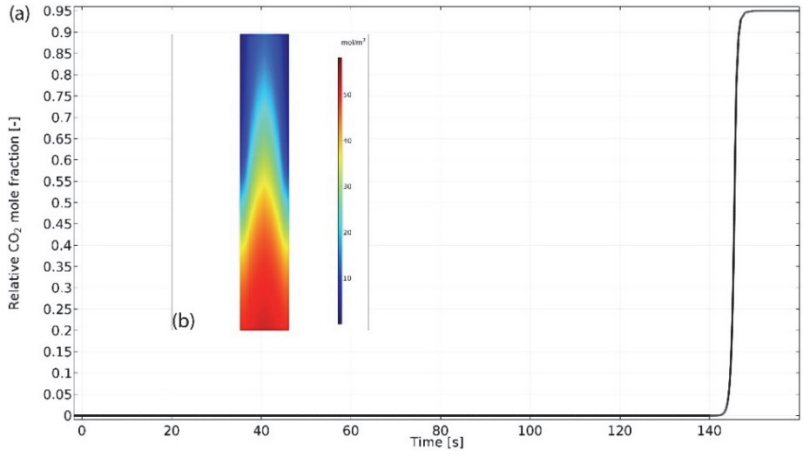

Fig. 5. CO_2 mole fraction at the reactor outlet relative to CO_2 mole fraction of the feed gas calculated by the CFD model with a dynamic k_{LDF} (a) and CO_2 surface flow profile (b)

Table 6. Structured bed model predictions

Total adsorbent mass [kg]	*Breakthrough time [s]*	*Loading at breakthrough [kg/mol]*	*CO_2 molar flow rate [mol s^{-1}]*	*Stoichiometric breakthrough time [s]*	*Pressure drops [Pa]*
0.765	141.38	0.36	0.00195	141.37	17.04

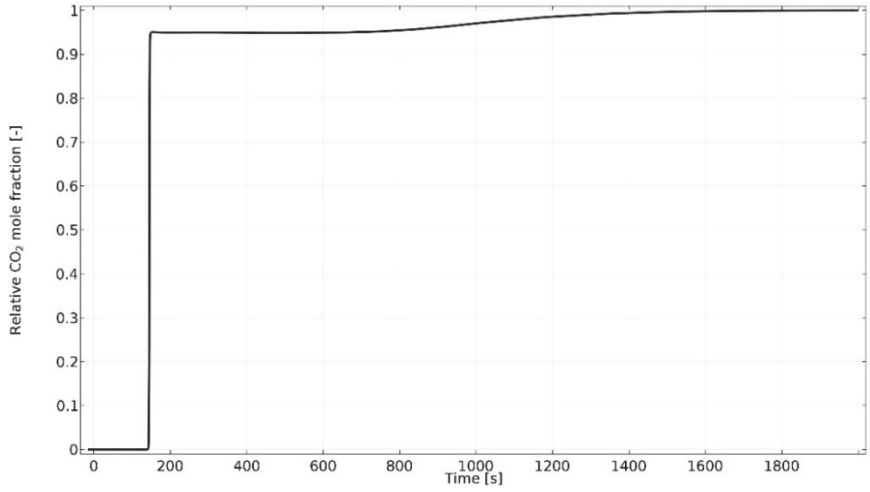

Fig. 6. CO_2 mole fraction at the reactor outlet relative to CO_2 mole fraction of the feed gas calculated by the CFD model with a dynamic k_{LDF} over a time period of 2000 s

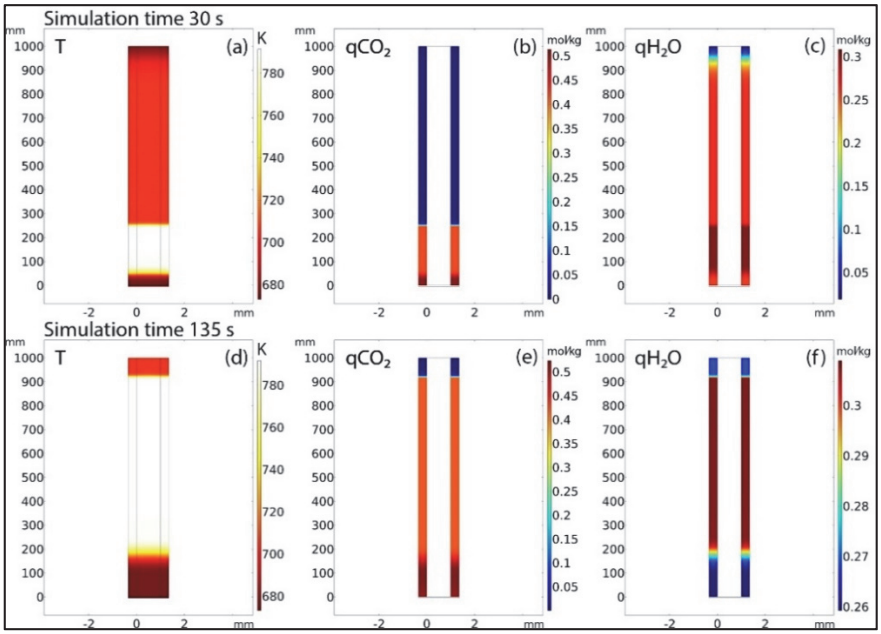

Fig. 7. Surface graphs at 30 s simulation time, before H_2O breakthrough, for temperature K (a), CO_2 loading mol kg^{-1} (b), H_2O loading mol kg^{-1} (c) and at 135 s, before CO_2 breakthrough, for temperature K (d), CO_2 loading mol kg^{-1} (e), H_2O loading mol kg^{-1} (f)

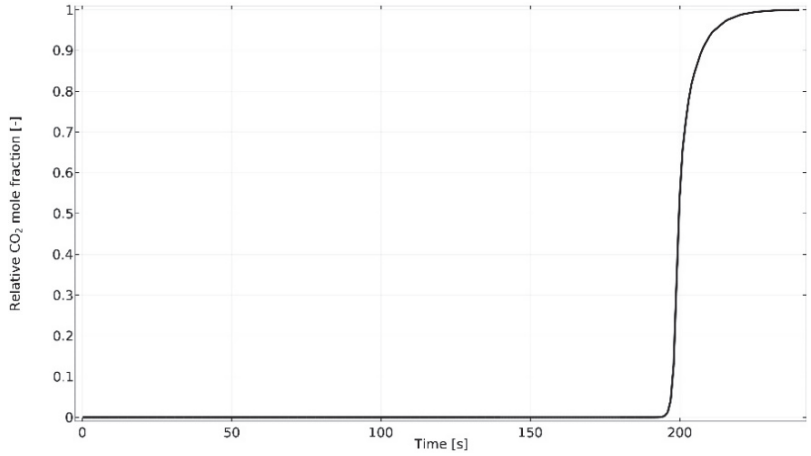

Fig. 8. CO_2 mole fraction at the reactor outlet relative to CO_2 mole fraction of the feed gas calculated by the isothermal CFD model with a dynamic k_{LDF}

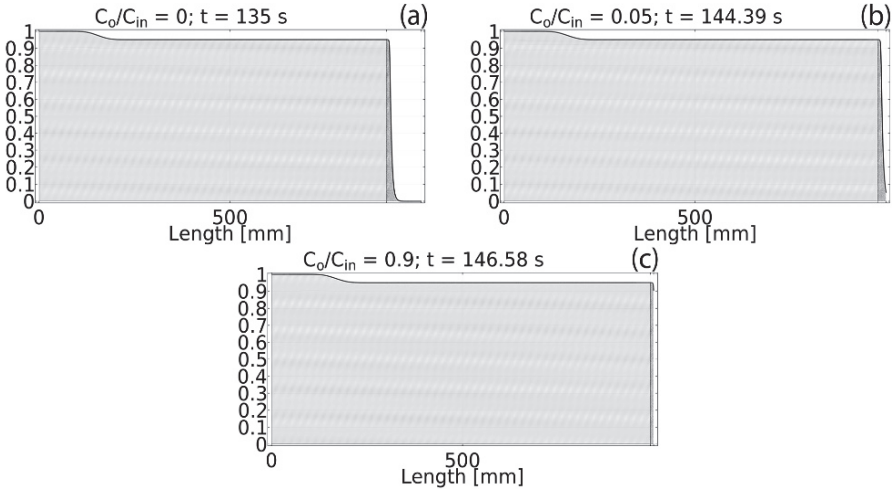

Fig. 9. MTZ behavior before breakthrough (a), at the beginning of breakthrough (b) and near the end of breakthrough (c); Grey area - saturated zone, dark grey area - adsorption zone (MTZ), white area - fresh adsorbent

It can be seen that the MTZs at different times are relatively short, evidence of high mass transfer rates and low mass transfer resistance. The breakthrough curve profile (Fig. 5a) can also be used for mass transfer assessment. The predicted breakthrough curve profile was steep, which is an indication of low transfer resistance and a very efficient utilization of the adsorbent bed (McCabe et al., 2004; Seader et al., 2011).

4. Conclusions

A multi-component competitive isotherm for CO_2 and H_2O was implemented in COMSOL Multiphysics and successfully validated using experimental data found in literature. The adsorption isotherm is composed of a first term that describes surface adsorption at lower pressures and a second term that reflects nanopore adsorption at higher pressures. The interaction seen at higher pressure values leads to the assumption of a competitive mechanism.

COMSOL Multiphysics was used to develop a 1D fixed bed model of adsorption of CO_2 in the SEWGS process. The model used the multi-component isotherm and the LDF approximation to describe adsorption. The model was successfully validated as breakthrough predictions were in agreement with predictions available in literature.

A novel approach to enhance SEWGS productivity, by replacing standard packed bed reactors with monolithic 3D-printed structures, was studied. To that end, a 2D CFD model of CO_2 and H_2O adsorption inside a single monolith reactor channel during the SEWGS process was developed. The developed dynamic model accounted for mass, heat and momentum transfer. The mesh density was sufficiently increased and error tolerance tightened until a favorable trade-off between computation time and accuracy of solution was reached. Predictions showed that heat transfer had a strong impact over adsorption capacity and reinforced the existence of a competitive adsorption mechanism highlighted by the isotherms. The development of an isothermal model confirmed the heat transfer effects. Although experimental validation was not possible due to the lack of any data available in literature, an analytical verification of the predicted loading amount was successfully carried out. Based on pressure drop values, steepness of the breakthrough curve profile and short size of the mass transfer zones, a preliminary assessment can be made that a structured bed configuration for SEWGS would provide more efficient mass transfer than traditional configurations.

Future work involves model transition from 2D to 3D, simulations of different channel geometries to study effects on mass transfer, development of a CFD fixed bed model for proper comparisons and experimental validation.

Acknowledgements

This work was supported by a grant of the Romanian National Authority for Scientific Research and Innovation, CCCDI - UEFISCDI, project number COFUND-ACT ERANET–3D-CAPS (contract number: 87/2017): "*3D Printed Capture Materials for Productivity Step-Change*", within PNCDI III.

Nomenclature

A	nanopore-sorbate interaction parameter, -
c	bulk concentration, mol m^{-3}
c_p	adsorbed concentration, mol kg^{-1}
C_p	specific heat capacity, J kg^{-1} K^{-1}
d	channel diameter, m
d_p	particle diameter, m
d_R	reactor diameter, m
D_m	molecular diffusion coefficient, m^2 s^{-1}
D_p	intraparticle diffusion coefficient, m^2 s^{-1}
D_s	surface diffusion coefficient, m^2 s^{-1}
D_s^0	surface diffusion coefficient at zero coverage, m^2 s^{-1}
E	nanopore-sorbate interaction energy, J mol^{-1}
h	bed height, m
ΔH	adsorption enthalpy, J mol^{-1}
i	species index, -
k_{LDF}	LDF intraparticle mass transfer coefficient, s^{-1}
k_p	adsorption isotherm, m^3 kg^{-1}
K	surface-sorbate interaction parameter, MPa^{-1}
K_m	porous material permeability, m^2
L	reactor length, m
L_{inlet}	inlet section length, m
m	pore-size distribution parameter, -
n	Freundlich isotherm parameter, -
nc	monolith channels number, -
p	pressure, Pa
p_c	critical pressure, Pa
p_f	feed pressure, Pa
p_0	saturation pressure, Pa
q_i	species excess amount adsorbed, mol kg^{-1}
q^*	equilibrium amount adsorbed, mol kg^{-1}
q^s	maximum (monolayer) amount adsorbed, mol kg^{-1}
q	conductive heat flux, W m^{-2}
q_0	convective heat flux, W m^{-2}
Q_V	volumetric flow rate, SL min^{-1}
r_i	inner radius of hollow cylinder, m
r_o	outer radius of hollow cylinder, m
R	gas constant, J mol^{-1} K^{-1}
R_{ADS}	adsorption rate expression, mol m^{-3} s^{-1}
t	time, s
t^*	stoichiometric breakthrough time, s
T	temperature, K
T_f	feed temperature, K
T_c	critical temperature, K
u	velocity, m s^{-1}
u_f	feed velocity, m s^{-1}
V_0	limiting nanopore volume per mass of sorbent, cm^3 kg^{-1}
w	half of total wall thickness, m
wt	wall thickness per channel, m
y	mole fraction, -

Greek symbols

q	conductive heat flux, W m^{-2}
q_0	convective heat flux, W m^{-2}

Q_V	volumetric flow rate, SL min^{-1}
r_i	inner radius of hollow cylinder, m
r_o	outer radius of hollow cylinder, m
R	gas constant, J mol^{-1} K^{-1}
R_{ADS}	adsorption rate expression, mol m^{-3} s^{-1}
t	time, s
t^*	stoichiometric breakthrough time, s

Abbreviations

CCS	carbon capture and storage
CFD	computational fluid dynamics
GHG	greenhouse gas
K-HTC	potassium promoted hydrotalcite
LDF	linear driving force
MTZ	mass transfer zone
PSA	pressure swing adsorption
SEWGS	sorption-enhanced water-gas shift
SMR	steam methane reforming

References

Bauer T., Guettel R., Roy S., Schubert M., Al-Dahhan M., Lange R., (2005), Modelling and simulation of the monolithic reactor for gas-liquid-solid reactions, *Chemical Engineering Research and Design*, **83**, 811-819.

Bertrand F., Devals C., Vidal D., Préval C.S. de, Hayes R.E., (2012), Towards the simulation of the catalytic monolith converter using discrete channel-scale models, *Catalysis Today*, **188**, 80-86.

Boger T., Heibel A.K., Sorensen C.M., (2004), Monolithic catalysts for the chemical industry, *Industrial & Engineering Chemistry Research*, **43**, 4602-4611.

Boon J., Cobden P.D., van Dijk H.A.J., Hoogland C., van Selow E.R., van Sint Annaland M., (2014), Isotherm model for high-temperature, high-pressure adsorption of CO_2 and H_2O on K-promoted hydrotalcite, *Chemical Engineering Journal*, **248**, 406-414.

Boon J., Cobden P.D., van Dijk H.A.J., van Sint Annaland M., (2015), High-temperature pressure swing adsorption cycle design for sorption-enhanced water-gas shift, *Chemical Engineering Science*, **122**, 219-231.

Chen J., Yang H., Wang N., Ring Z., Dabros T., (2008), Mathematical modeling of monolith catalysts and reactors for gas phase reactions, *Applied Catalysis A: General*, **345**, 1-11.

Coenen K., Gallucci F., Pio G., Cobden P., van Dijk E., Hensen E., van Sint Annaland M., (2017), On the influence of steam on the CO_2 chemisorption capacity of a hydrotalcite-based adsorbent for SEWGS applications, *Chemical Engineering Journal*, **314**, 554-569.

Dai C., Lei Z., Zhang J., Li Y., Chen B., (2013), Monolith catalysts for the alkylation of benzene with propylene, *Chemical Engineering Science*, **100**, 342–351.

Dhanushkodi S.R., Mahinpey N., Wilson M., (2008), Kinetic and 2D reactor modeling for simulation of the catalytic reduction of NO_x in the monolith honeycomb reactor, *Process Safety and Environmental Protection*, **86**, 303–309.

Do D.D., (1998), *Adsorption Analysis: Equilibria and Kinetics*, vol. 2, Imperial College Press, London, UK.

Durán Martínez F.L., Julcour C., Billet A.-M., Larachi F., (2016), Modelling and simulations of a monolith reactor for three-phase hydrogenation reactions - Rules and recommendations for mass transfer analysis, *Catalysis Today*, **273**, 121–130.

Ebner A.D., Reynolds S.P., Ritter J.A., (2006), Understanding the adsorption and desorption behavior of CO_2 on a K-promoted hydrotalcite-like compound (HTlc) through nonequilibrium dynamic isotherms, *Industrial & Engineering Chemistry Research*, **45**, 6387-6392.

Govender S., Friedrich H., (2017), Monoliths: a review of the basics, preparation methods and their relevance to oxidation, *Catalysts*, **7**, 1-29.

Hatch C.D., Wiese J.S., Crane C.C., Harris K.J., Kloss H.G., Baltrusaitis J., (2012), Water adsorption on clay minerals as a function of relative humidity: application of BET and Freundlich adsorption models, *Langmuir*, **28**, 1790-1803.

Heidebrecht P., Pfafferodt M., Sundmacher K., (2011), Multiscale modelling strategy for structured catalytic reactors, *Chemical Engineering Science*, **66**, 4389-4402.

Hufton J.R., Mayorga S., Sircar S., (1999), Sorption-enhanced reaction process for hydrogen production, *AIChE Journal*, **45**, 248-256.

IPCC, (2005), *Carbon Dioxide Capture and Storage*, report, Prepared by Working Group III of the Intergovernmental Panel on Climate Change, Cambridge, England.

IPCC, (2014), *Climate Change 2014: Synthesis Report*, report, Contribution of Working Groups I, II and III to the Fifth Assessment Report of the Intergovernmental Panel on Climate Change, Geneva, Switzerland.

Irani M., Alizadehdakhel A., Pour A.N., Hoseini N., Adinehnia M., (2011), CFD modeling of hydrogen production using steam reforming of methane in monolith reactors: Surface or volume-base reaction model? *International Journal of Hydrogen Energy*, **36**, 15602–15610.

Jang H.M., Lee K.B., Caram H.S., Sircar S., (2012), High-purity hydrogen production through sorption enhanced water gas shift reaction using K_2CO_3-promoted hydrotalcite, *Chemical Engineering Science*, **73**, 431-438.

Le Treut H., Sommerville R., Cubasch U., Ding Y., Mauritzen C., Mokssit A., Peterson T., Prather M., (2007), *Historical Overview of Climate Change Science*, In: *Climate change 2007: the physical science basis. Contribution of Working Group I to the Fourth Assessment Report of the Intergovernmental Panel on Climate Change*, Cambridge University Press, Cambridge, UK and New York, USA, 95-122.

Lee J.M., Min Y.J., Lee K.B., Jeon S.G., Na J.G., Ryu H.J., (2010), Enhancement of CO_2 sorption uptake on hydrotalcite by impregnation with K_2CO_3, *Langmuir*, **26**, 18788-18797.

Lee K.B., Beaver M.G., Caram H.S., Sircar S., (2008), Reversible chemisorbents for carbon dioxide and their potential applications, *Industrial & Engineering Chemistry Research*, **47**, 8048-8062.

Lee K.B., Verdooren A., Caram H.S., Sircar S., (2007), Chemisorption of carbon dioxide on potassium-carbonate-promoted hydrotalcite, *Journal of Colloid and Interface Science*, **308**, 30-39.

Lei Z., Guo Y., Dai C., Zi L., Chen B., (2016), Simulation of hydrodynamic and mass transfer performances in monolith channel, *Catalysis Today*, **276**, 150-160.

Lupše J., Campolo M., Soldati A., (2016), Modelling soot deposition and monolith regeneration for optimal design of automotive DPFs, *Chemical Engineering Science*, **151**, 36-50.

Maroño M., Torreiro Y., Gutierrez L., (2013), Influence of steam partial pressures in the CO_2 capture capacity of K-doped hydrotalcite-based sorbents for their application to SEWGS processes, *International Journal of Greenhouse Gas Control*, **14**, 183-192.

Maroño M., Torreiro Y., Montenegro L., Sánchez J., (2014), Lab-scale tests of different materials for the selection of suitable sorbents for CO_2 capture with H_2 production in IGCC processes, *Fuel*, **116**, 861-870.

McCabe W.L., Smith J.C., Harriott P., (2004), *Unit Operations of Chemical Engineering*, 7th Edition, McGraw-Hill Education, New York, NY.

Pahinkar D.G., Garimella S., (2018), A novel temperature swing adsorption process for natural gas purification: Part I, model development, *Separation and Purification Technology*, **203**, 124-142.

Patton A., Crittenden B.D., Perera S.P., (2004), Use of the linear driving force approximation to guide the design of monolithic adsorbents, *Chemical Engineering Research and Design*, **82**, 999-1009.

Pramanik S., Ravikrishna R.V., (2017), Numerical study of rich catalytic combustion of syngas, *International Journal of Hydrogen Energy*, **42**, 16514-16528.

Reijers H.T.J., Boon J., Elzinga G.D., Cobden P.D., Haije W.G., van den Brink R.W., (2009), Modeling study of the sorption-enhanced reaction process for CO_2 capture. I. Model development and validation, *Industrial & Engineering Chemistry Research*, **48**, 6966-6974.

Reijers H.T.J., Boon J., Elzinga G.D., Cobden P.D., Haije W.G., Van Den Brink R.W., (2009), Modeling study of the sorption-enhanced reaction process for CO_2 capture. II. Application to steam-methane reforming, *Industrial and Engineering Chemistry Research*, **48**, 6975-6982.

Riboldi L., Bolland O., (2017), Overview on pressure swing adsorption (PSA) as CO_2 capture technology: state-of-the-art, limits and potentials, *Energy Procedia*, **114**, 2390-2400.

Rodríguez M.L., Cadús L.E., Borio D.O., (2016), VOCs abatement in adiabatic monolithic reactors: Heat effects, transport limitations and design considerations, *Chemical Engineering Journal*, **306**, 86-98.

Sadeghi F., Tirandazi B., Khalili-Garakani A., Nasseri S., Nabizadeh Nodehi R., Mostoufi N., (2017), Investigating the effect of channel geometry on selective catalytic reduction of NO_x in monolith reactors, *Chemical Engineering Research and Design*, **118**, 21-30.

Seader J.D., Henley E.J., Roper D.K., (2011), *Separation Process Principles. Chemical and Biochemical Operations*, 3rd Edition, Wiley, Hoboken, NJ.

Sharma A.K., Birgersson E., (2016), Validity and scalability of an asymptotically reduced single-channel model for full-size catalytic monolith converters, *Applied Mathematics and Computation*, **281**, 186-198.

Sikander U., Sufian S., Salam M.A., (2017), A review of hydrotalcite based catalysts for hydrogen production systems, *International Journal of Hydrogen Energy*, **42**, 19851-19868.

Tischer S., Deutschmann O., (2005), Recent advances in numerical modeling of catalytic monolith reactors, *Catalysis Today*, **105**, 407-413.

van Selow E.R., Cobden P.D., van den Brink R.W., Hufton J.R., Wright A., (2009), Performance of sorption-enhanced water-gas shift as a pre-combustion CO_2 capture technology, *Energy Procedia*, **1**, 689-696.

van Selow E.R., Cobden P.D., van Dijk H.A.J., Walspurger S., Verbraeken P.A., Jansen D., (2013), Qualification of the ALKASORB sorbent for the sorption-enhanced water-gas shift process, *Energy Procedia*, **37**, 180-189.

van Selow E.R., Cobden P.D., Wright A.D., van den Brink R.W., Jansen D., (2011), Improved sorbent for the sorption-enhanced water-gas shift process, *Energy Procedia*, **4**, 1090-1095.

Voldsund M., Jordal K., Anantharaman R., (2016), Hydrogen production with CO_2 capture, *International Journal of Hydrogen Energy*, **41**, 4969-4992.

Walspurger S., Cobden P.D., Safonova O.V., Wu Y., Anthony E.J., (2010), High CO_2 storage capacity in alkali-promoted hydrotalcite-based material: In situ detection of reversible formation of magnesium carbonate, *Chemistry – A European Journal*, **16**, 12694-12700.

Winter C.J., (2009), Hydrogen energy — abundant, efficient, clean: A debate over the energy-system-of-change, *International Journal of Hydrogen Energy*, **34**, S1-S52.

Wood G.O., (2002), Quantification and application of skew of breakthrough curves for gases and vapors eluting from activated carbon beds, *Carbon*, **40**, 1883–1890.

Wright A.D., White V., Hufton J.R., Quinn R., Cobden P.D., van Selow E.R., (2011), CAESAR: Development of a SEWGS model for IGCC, *Energy Procedia*, **4**, 1147-1154.

Yong Z., Mata V., Rodrigues A.E., (2002), Adsorption of carbon dioxide at high temperature - a review, *Separation and Purification Technology*, **26**, 195-205.

Zheng Y., Shi Y., Li S., Yang Y., Cai N., (2014), Elevated temperature hydrogen/carbon dioxide separation process simulation by integrating elementary reaction model of hydrotalcite adsorbent, *International Journal of Hydrogen Energy*, **39**, 3771-3779.

Zivkovic S., Vukadinovic B., Veljkovic M., (2018), Cleaner and energy efficient production: a case study, *Environmental Engineering and Management Journal*, **17**, 175-188.